Effect of clamped beam pattern on resonant frequency shift of microresonator under near-infrared laser irradiation

Takegami, Kohei ; Nakafuji, Kota ; Arai, Naoyuki ; Uesugi, Akio ; Sugano, Koji ; Isono, Yoshitada

(Citation)
Japanese Journal of Applied Physics,59(SI):SIII04

(Issue Date)
2020-06

(Resource Type)
journal article

(Version)
Accepted Manuscript

Effect of clamped beam pattern on resonant frequency shift of microresonator under near-infrared laser irradiation

Kohei Takegami, Kota Nakafuji, Naoyuki Arai, Akio Uesugi, Koji Sugano, and Yoshitada Isono

Department of Mechanicak Engineering, Graduate school of Engineering, Kobe University, 1-1 Rokkodai-cho, Nada-ku, Kobe 657-8501 JAPAN

E-mail: sugano@mech.kobe-u.ac.jp

In this study, we investigated the effect of the resonator beam shape on the thermal stress and the resonance frequency change when providing heat to the resonator beam by near-infrared laser irradiation. This investigation provides crucial data for optical and heat sensing application using microresonators. The microresonator beam with an optical absorber for near-infrared region was fabricated, varying the numbers of beams and corners. When irradiating the optical absorber with a laser, the resonant frequency decreased. It is because the photothermal effect provides compressive stress in the beam, resulting in resonant frequency decrease. The resonant frequency change rate increased with decreasing the number of beams. According to the analytical results, we confirmed that the analytical thermal stress determined the resonant frequency change rate in the same beam length. The corner remarkably decreased the resonant frequency change rate. The straight beams bend to the orthogonal direction by the thermal expansion of another straight part of the beam, resulting in deformation of the beam in the axial direction. Therefore, the reaction force and compressive stress in the axial direction reduces.

1. Introduction

The silicon (Si)-based MEMS (Microelectromechanical systems) technology has been employed for the development of uncooled bolometer-based infrared sensors.[1-3] The bolometer has been used for infrared thermal sensing of automotive applications and so on. These sensors give us many advantages such as low cost and miniaturization against compound semiconductors because of Si-based MEMS fabrication process. A sensitivity enhancement of bolometers is demanded to extend the application. Another approach is an MEMS resonator, which provides us an ultimate sensitivity such as mass sensing and so on because the resonant frequency is sensitive to mass, ambient pressure, temperature, and so on.[4-12] A resonator-based infrared sensing with a quartz[13,14] or a piezoelectric thin film of Aluminum nitride (AlN)[15-20] has been reported so far. The Si-based resonator has advantages of compatibility with CMOS and Si MEMS fabrication, and higher quality (Q) factor of single crystalline material. A wide range of wavelengths, including near-infrared region of more than around 1100 nm, have recently become crucial for many applications instead of indium gallium arsenide (InGaAs) detectors. Near-infrared detectors using a clamped resonator have also been reported so far.[21,22] In these studies, the following principle is used to transduce optical input to resonant frequency shift.[23,24] An optical input to a resonator beam generates heat by photothermal conversion resulting in a temperature rise of the resonator beam. The temperature rise causes the thermal stress of the resonator beam. It leads to a resonant frequency shift.[25-27] The amount of the input heat and optical intensity is measurable from the resonant frequency shift. A compressive stress leads to lower resonant frequency. This principle is expected for Si-based optical sensors with high sensitivity. This principle can also be applied to thermal sensing.[28,29] For higher sensitivity, in the case of clamped beams, we have to consider two points of high temperature and high compressive stress of beams. High temperature is realized by low heat conduction of beams, namely longer beam with smaller cross-sectional area, which will be expressed in the theoretical section. The temperature and shape of the beam has an effect on compressive stress. The beam pattern design of the microresonator is significantly essential for highly sensitive optical sensors.

We consider not only sensing applications but also actuating applications. A resonant frequency shift of resonators by laser irradiation has also been applied for resonant frequency tuning.[30] On the other hand, resonant actuators such as a micromirror have a problem of resonant frequency shift due to light irradiation or ambient temperature change. The compressive or tensile stress due to the temperature change of the whole device chip

including a package causes resonant frequency shift. For these issues, a resonant frequency shift should be suppressed.

From these viewpoints, in this study, we investigated an effect of beam pattern on resonant frequency shift. We fabricated the clamped resonator beam with an optical absorber. This study used two kinds of beam patterns. One is a straight beam with a different number of beams, and another is a combination of plural beams with a different number of corners. We investigated the effects of corners, thermal stress, and deformation of beams on resonant frequency shift experimentally and analytically.

2. Principle and device structure

2.1 Principle and theoretical equations

A schematic diagram of the Si microresonator device used in this study is shown in Fig. 1(a). The device was fabricated from an SOI (silicon on insulator) wafer. The device consists of the clamped beam, the optical absorber located at the beam center, and the through-hole. The beam vibrates in an out-of-plane direction. A laser was irradiated to the optical absorber so that the beam temperature rises. It produces a compressive thermal stress to a clamped beam. It results in a shift of mechanical resonant frequency of the beam.

For simplicity of a theoretical equation, we consider the straight beam with a uniform cross-sectional area shown in Fig. 1(b) and (c) as a model for a theoretical equation. Temperature change ΔT when a laser with an intensity P is irradiated to the center ($x = 0$) of the beam with length l, width w, and thickness t is represented as the following equation.

$$\Delta T = \int_{-l/2}^{l/2} \frac{(l/2 - |x|)\beta P}{\kappa w t} \frac{dx}{l} = \frac{l \Delta \beta P}{8 w t \kappa} \ . \tag{1}$$

Here, κ is thermal conductivity, and we adopt absorption $\Delta\beta$ to the optical absorber. Thermal stress change $\Delta\sigma$ due to temperature change ΔT is calculated using the following equation.

$$\Delta\sigma = -\alpha E \Delta T = -\frac{\alpha E l \Delta \beta P}{8 w t \kappa} \ . \tag{2}$$

Here, E and α is young's modulus and thermal expansion coefficient, respectively. Finally, we obtain resonant frequency f_λ under laser irradiation P and resonant frequency change rate $\Delta f/f_0$ as follows.

$$f_\lambda = f_0 \sqrt{1 + \frac{3\Delta\sigma l^2}{\pi^2 E t^2}} = f_0 \sqrt{1 - \frac{3\alpha l^3 \beta P}{8\pi^2 t^3 w \kappa}} \approx f_0 \left(1 - \frac{3\alpha l^3 \beta P}{16\pi^2 t^3 w \kappa}\right) \ . \tag{3}$$

$$\frac{\Delta f}{f_0} = \frac{f_\lambda - f_0}{f_0} \approx -\frac{3\alpha l^3}{16\pi^2 t^3 w \kappa} \beta P \ . \tag{4}$$

Here f_0 is original resonant frequency under no laser irradiation. We obtained the following properties from the equations described above. Resonant frequency f_λ decreases with laser intensity P. Resonant frequency change rate $\Delta f/f_0$ is linearly proportional to temperature change ΔT, laser intensity P, a cube of beam length l, and inversely proportional to beam width w. Temperature change ΔT is linearly proportional to beam length l.

2.2 Beam pattern

Figure 2(a) shows an example of the resonator pattern. The resonator is structured such that beams support the center pad. The resonator length is determined by the size of the through-hole provided in the buried oxide (BOX) layer of the SOI wafer. The width w and the thickness t of the beam were 10 μm and 1.5 μm, respectively. The BOX layer thickness is 0.25 μm. The size of the center pad and the absorber were set to 40 μm × 40 μm and 20 μm × 20 μm, respectively.

We designed two kinds of device structures in order to investigate the effect of the resonator beam shape on the thermal stress and resonance frequency change, as shown in Fig. 3. One is the resonator pattern with the different number of supporting beams between the center pad and the fixed ends. The device is named “Device A”. We fabricated one beam (A1), two beams (A2), and three beams (A3) for one side, as shown in Fig. 3 (A1)-(A3). One beam length is 180 μm. Another is the resonator pattern with the different number of corners in supporting beams, as shown in Fig. 3 (B1)-(B9). This device has two supporting beam for one side based on the device A2. The device is named “device B”. The number of corners varied to 0 (A2), 1 (B1), 2 (B2), 3 (B3), 4 (B4), 5 (B5), 8 (B8), and 9 (B9) for one beam. We designed the beam length as shown in Fig. 3(c). The sum of the straight part in one beam is constant (180 μm) for all devices.

2.3 Device fabrication

The device was fabricated using the standard MEMS fabrication process as follows. The fabrication started from the SOI wafer. (a) The pattern of gold thin film with a thickness of 100 nm was fabricated by photolithography and subsequent electron beam (EB) vacuum evaporation for the lift-off process. Gold nanowires were fabricated using an EB lithography based lift-off process. A sputtered Si was deposited and then patterned for gold nanowire covering. (b) The through-hole was fabricated by deep-RIE (reactive ion etching) from the backside of the Si substrate. (c) The resonator beam structure was patterned by Si etching. (d) The BOX layer was removed by buffered hydrofluoric acid (BHF) from the backside of the through-hole. Figure 4 shows the SEM images of the fabricated devices.

2.4 Optical absorber

A gold nanowire structure was located at the center of the device as an absorber for photothermal conversion in the near-infrared region. The designed width, height, and pitch of gold nanowires were 100 nm, 50 nm, and 750 nm. The thickness of the coating Si was approximately 118 nm. The sputtered Si was required in order to obtain absorption peaks in the near-infrared region.

Figure 5 shows the SEM images and the measured absorption spectrum of the absorber, corresponding to Fig. 2(b). The absorption shown in Fig. 5 was calculated subtracting the measured reflection from 100% because of the transmission of the gold thin film as shown in Fig. 2(c) is considered to be 0%. The absorption spectrum shows some peaks with high absorption in the near-infrared region.

3. Measurement and analytical method

3.1 Experimental method

The resonant frequency characteristics of the resonator device were measured with a laser Doppler vibrometer and a ceramic piezoelectric actuator. The device chip was put on a ceramic piezoelectric actuator in order to excite the resonator. A laser Doppler vibrometer using a He-Ne laser (wavelength 632.8 nm) was used for an amplitude measurement. It irradiated the Si surface of the center pad with a He-Ne laser. We used a wavelength-tunable laser to irradiate the absorber on the resonator beam. A lock-in amplifier (Zurich Instruments Ltd., MFLI) was used to control the applied voltage to the ceramic piezoelectric actuator and to obtain the output signal from the laser Doppler vibrometer. The device chip was put in a vacuum chamber at a pressure of 10^{-2} Pa or less. The laser intensity to the absorber was controlled to 1, 0.9, 0.8, 0.7, 0.6, 0.5, and 0 mW at the laser wavelength of 1530 nm. The excitation voltage of the ceramic piezoelectric actuator was set to 4 mV. We swept excitation frequency and then acquired the first-appeared resonant frequency in each measurement, indicating the resonant frequency of the primary mode. In order to accurately analyze the resonance peak from the frequency response curve obtained in this experiment, fitting was performed using the Lorentzian function.

3.2 Analytical method

In order to investigate the effect of the resonator shape on the thermal stress and resonance frequency change, we calculated the thermal stresses generated by laser irradiation and the resonant frequency shifts of each device by FEM (Finite Element Method) simulation. The calculation method is explained below.

Heat conduction, thermal stress, and resonant mode analyses were performed using the commercially available FEM software. The analysis model was simplified to the freestanding beam part of the device. The design dimension was used for the dimensions of FEM models. The both ends of the beam were mechanically fixed. The temperature at the fixed ends was set to 27 ºC (300 K). A heat generation region, which is the size of the gold nanostructure, was set on the pad surface of 25 μm×25 μm in the center of the pad. We set the heat input of 0.4 mW to the absorber, corresponding to P=1 mW laser irradiation and β=40% absorption to the absorber.

Then we explain the characterization method for thermal stress using the schematics of the device B1 as shown in Fig. 6. The thermal stresses in an axial direction at the left, center, and right points on the cross-section of the beam were extracted from the calculation results. The three points of left edge, center, and right edge were set to the center in the thickness direction. Then an average of three points was calculated except for the corner part. The total average of stress was also calculated for each device.

4. Results and discussion

4.1 Experimental results

Figure 7(a) shows the measurement results of resonance curves when the device with two straight beam at one side (A2) was irradiated with a laser from 0.5 to 1 mW of intensity. The resonance peak shifted to lower frequency with increasing the laser intensity. It is because compressive stress was applied to the beam by temperature rise.

Figure 7(b) shows the resonant frequencies of each device (A1, A2, and A3) as a function of the laser intensity P mW. The resonant frequency decreased linearly with increasing the laser intensity. The experimental results show the same tendency as the theoretical equation (Eq. (3)). It is because of thermal compressive stress linearly increased with laser intensity (Eq. (2)). Figure 7(c) shows the resonant frequency change rate, which was defined by Eq. (4), depending on the laser intensity. The resonant frequency change rate increased linearly as the laser intensity increased. This tendency is also consistent with the theoretical equation (Eq. (4)). The slope of decrease in resonant frequency varied depending on the number of beams. Figure 7(d) shows the resonant frequency change rate as a function of the number of beams when irradiating with a 1 mW laser. The measured change rate of the resonant frequency was inversely proportional to the number of beams. The experimental results indicate the same tendency as the theoretical equation of Eq. (4) because the increase in the number of beams indicates the increase in width of beam w resulting in low thermal

conduction and higher temperature.

Figure 8(a) shows the resonant frequency change rate as a function of the number of corners when irradiating the device B with a 1 mW laser. The original resonance frequencies f_0 of the device B1-B9 were 128.8, 99.1, 132.3, 107.9, 112.9, 75.4, and 68.3 kHz, respectively. The resonant frequency decreased with increasing the number of corners in the calculation because the actual length of a beam increased when including the square at the corner as shown in Fig. 3. According to the SEM images shown in Fig. 4, however, the length of the fabricated beams became shorter than the design model because the through hole became small. The error of the device 1, 3, and 5 was significant. The resonant frequency change rate increased linearly with laser intensity. Comparing the device A2 without a corner to the device B1 with a corner, the resonant frequency change rate significantly reduced by a corner in the beam, as shown in Fig. 8(b). The resonance frequency change rate of the device B1 with one corner showed -1.48×10^{-3} indicating 98.8% decrease from -125×10^{-3} of the device A2 without a corner. The resonant frequency change rate increased with increasing the number of corners from one (B1) to nine (B9).

4.2 Analytical results

First, the analytical results of thermal stress distribution of the device B1 and A2 are shown. Figure 9 shows the FEM analysis results of the thermal stress at three points on the cross-sectional area of the beam as a function of distance from the start point, as shown in Fig. 6. The data of the upper right beam was used in four beams. Positive and negative values indicate tensile and compressive stresses, respectively. The average stress of the three points at the left edge, center, and right edge of each distance was calculated. The average stresses of 3 points of device B1 and A2 along the axial direction were also shown in Fig. 9. Figure 10 shows the average stress of 3 points and the total average of all stress data of each device. Figure 11 shows contour plots of deformation due to thermal expansion of B1 and A2.

According to Fig. 9(a) for the device B1, the compressive and tensile stresses at the left and right edges switches at the distances of approximately 38 and 128 μm. A protruding thermal compressive stress appears at the left edge beside the corners at the distance of 90 μm from the start point, as shown in Fig. 9(a). The stress at the left and right edges of the beam shows the compressive and tensile stresses at each position according to the deformation of the beam. The compressive and tensile stresses of the left and right edges were canceled out each other. The average stress along the axial direction at the straight part of the beam was almost the same as the stress at the center. We calculated the total average of the average cross-sectional stress for each device. The total average stress was calculated

to be −27.8 kPa, and it was similar to the stress of −29.1 kPa taking from the straight part of the beam, as shown in Fig. 10(a).

On the other hand, the device A2 without a corner has only compressive stress, as shown in Fig. 9(b). The stress distribution of A2 was similar to that of B1. No protruding stress was observed because of no corner. The stress at the center is representative. The total average of the stress also can express the device stress, as shown in Fig. 10(b) as well as the device B1. The total average of the device A2 was −1.94 MPa, and it was much larger than that of the device B1. Figure 7(d) also shows the analytical results on the resonant frequency change rate and thermal stress. The experimental resonant frequency change rate of the device A was in good agreement with the analytical results. We consider the small difference between them is because of the dimensional error in the fabrication. It shows the same tendency as the total average of the thermal stress. We confirmed that the total average of the thermal stress could be used for the evaluation of the resonant frequency change rate. According to Fig. 8(b), the experimental results of B1 (1 corner) and A2 (0 corner) show good agreement with each other and the same tendency as the total average of the thermal stress.

Figure 12 shows the average thermal stresses of the devices B1, B2, and B3 as a function of distance from the start point. The stress distributions of the devices B1, B2, and B3 are similar. A protruding thermal compressive stress beside corners were observed. The constant stress at the straight part of the beam was observed in the devices B2 and B3 data as well as the device B1. The constant stress increased with the number of corners. As shown in Fig. 8(b), the experimental and the analytical resonant frequency change rate, and the total average of the thermal stress show a similar tendency. The differences of resonant frequency in the device B between the experimental and the analytical results were larger than that of the device A. The reason is thought to be also the dimensional error as the device A. However the error is more significant when a through hole design is small, resulting in a smaller hole than the model. It leads to a shorter length beam as mentioned in 4.1. The dimensional error has a small influence on the resonant characteristics. However, the tendency of the resonant frequency change rate shows good agreement with the calculation. In order to discuss the effect of corners, the dimensional error is not significant.

4.3 Discussion

In this section, we discuss the relationship between the total average of thermal stress and the resonant frequency change rate.

The much lower change rate of the resonant frequency of the device B1 is because

of lower compressive stress than that of the device A2. According to Fig. 11(a), the straight beams bend to the orthogonal direction by the thermal expansion of another straight part of the beam, resulting in the deformation of the beam in the axial (longitudinal) direction. Therefore, the reaction force and compressive stress in the axial direction reduces. According to the deformation shown in Fig. 11(b), the beams bend outward because of the central pad expansion. However, the deformation in the axial direction is small enough to hold compressive stress in the axial direction. In the device A2, the deformation of orthogonal direction can be ignored for the resonant frequency change rate.

According to Fig. 8(b), the resonant frequency change rate and the total average of thermal stress increased with the number of corners from one (B1) to nine (B9). We consider that it is because of temperature increases with the number of corners. We designed the dimension of the device B so that the total length of the straight part of one beam from the central pad is 180 μm, excepting the corners. Figure 13 shows the maximum temperature in the beam calculated by FEM simulation when the number of beam corners varied. The maximum device temperature increased linearly as the number of corners increased, resulting in thermal stress increase. This is because the actual length of a beam increased with the number of beams when including the square at the corner. The temperature increases with the length as shown in Eq. (1). That is the reason why the resonant frequency change rate and the thermal compressive stress increased with the number of corners.

5. Conclusions

In this study, in order for optical sensing and actuating application of a microresonator device, effects of the number of beams and the number of corners were experimentally and analytically investigated. As an experimental result, it was confirmed that the resonance frequency decreased as the laser intensity increased. It is because compressive stress was applied to the beam by temperature rise. The measured change rate of the resonant frequency was inversely proportional to the number of beams because of lower thermal conduction and higher temperature of the beam. The resonance frequency change rate of the device B1 showed -1.48×10^{-3} indicating 98.8% decrease from -125×10^{-3} of the device A2. It is because the total average of the device B1 was −27.8 kPa, and it was much lower than −1.94 MPa of the device A2. The straight beams bend to the orthogonal direction by the thermal expansion of another straight part of the beam, resulting in deformation of the beam in the axial direction. Therefore, the reaction force and compressive stress in the axial direction reduces. The resonant frequency change rate and the total average

of thermal stress increased with the number of corners from one (B1) to nine (B9). We consider that it is because of temperature increases with the number of corners. We confirmed that the corner in the resonator beam has considerable effects on the response of resonant frequency shift to light or heat input.

Acknowledgment

Part of this study was supported by the Kyoto University Nano Technology Hub in the "Nanotechnology Platform Project", sponsored by the Ministry of Education, Culture, Sports, Science, and Technology, Japan (MEXT).

References

1) S. Ogawa and M. Kimata, Materials (Basel), **10** (2017).
2) M. Kimata, IEEJ Transactions on Electrical and Electronic Engineering, **13**, 4 (2018).
3) S. Ogawa and M. Kimata, Materials (Basel), **11** (2018).
4) K. Y. Yasumura, T. D. Stowe, E. M. Chow, T. Pfafman, T. W. Kenny, B. C. Stipe, and D. Rugar, Microelectromechanical Systems, Journal of, **9**, 117 (2000).
5) A. N. Cleland and M. L. Roukes, Journal of Applied Physics, **92**, 2758 (2002).
6) J. Yang, T. Ono, and M. Esashi, Microelectromechanical Systems, Journal of, **11**, 775 (2002).
7) X. Li, T. Ono, Y. Wang, and M. Esashi, Applied Physics Letters, **83**, 3081 (2003).
8) T. Ono, X. Li, H. Miyashita, and M. Esashi, Review of Scientific Instruments, **74**, 1240 (2003).
9) K. Ekinci, Y. Yang, and M. Roukes, Journal of applied physics, **95**, 2682 (2004).
10) T. Ono and M. Esashi, Measurement Science and Technology, **15**, 1977 (2004).
11) K. L. Ekinci and M. L. Roukes, Review of Scientific Instruments, **76**, 061101 (2005).
12) H. B. Peng, C. W. Chang, S. Aloni, T. D. Yuzvinsky, and A. Zettl, Phys Rev Lett, **97**, 087203 (2006).
13) J. R. Vig, R. Filler, and Y. Kim, Journal of Microelectromechanical Systems, **5**, 131 (1996).
14) P. Kao and S. Tadigadapa, Sensors and Actuators A: Physical, **149**, 189 (2009).
15) R. B. Karabalin, M. H. Matheny, X. L. Feng, E. Defaÿ, G. Le Rhun, C. Marcoux, S. Hentz, P. Andreucci, and M. L. Roukes, Applied Physics Letters, **95**, 103111 (2009).
16) Y. Hui, J. S. Gomez-Diaz, Z. Qian, A. Alu, and M. Rinaldi, Nat Commun, **7**, 11249 (2016).
17) Z. Qian, Y. Hui, F. Liu, S. Kang, S. Kar, and M. Rinaldi, Microsystems &

316 Nanoengineering, **2**, 16026 (2016).
317 18) Y. Hui and M. Rinaldi, Applied Physics Letters, **102**, 093501 (2013).
318 19) G. Piazza, P. J. Stephanou, and A. P. Pisano, Journal of Microelectromechanical
319 Systems, **15**, 1406 (2006).
320 20) V. Yantchev and I. Katardjiev, Journal of Micromechanics and Microengineering, **23**,
321 043001 (2013).
322 21) E. Maeda and R. Kometani, Applied Physics Letters, **111**, 013102 (2017).
323 22) K. Sugano, Y. Tanaka, E. Maeda, R. Kometani, and Y. Isono, Microresonator with
324 gold nanorod array for laser wavelength measurement by photo-thermal conversion,
325 2017, p. 159.
326 23) A. Bokaian, Journal of sound and vibration, **126**, 49 (1988).
327 24) A. Bokaian, Journal of sound and vibration, **142**, 481 (1990).
328 25) R. R. Syms, Microelectromechanical Systems, Journal of, **7**, 164 (1998).
329 26) T. Remtema and L. Lin, Sensors and Actuators A: Physical, **91**, 326 (2001).
330 27) S. C. Jun, X. M. H. Huang, M. Manolidis, C. A. Zorman, M. Mehregany, and J. Hone,
331 Nanotechnology, **17**, 1506 (2006).
332 28) N. Inomata, M. Toda, M. Sato, A. Ishijima, and T. Ono, Applied Physics Letters, **100**,
333 154104 (2012).
334 29) M. Toda, N. Inomata, T. Ono, and I. Voiculescu, IEEJ Transactions on Electrical and
335 Electronic Engineering, **12**, 153 (2017).
336 30) H. Okamoto, T. Kamada, K. Onomitsu, I. Mahboob, and H. Yamaguchi, Applied
337 Physics Express, **2**, 062202 (2009).
338
339

Figure Captions

Fig. 1. Overview of a resonator vibrates in the out-of-plane direction by external excitation. An optical absorber is mounted on the center of the beam. (a) Schematic of the device fabricated from an SOI wafer. (b) A-A' cross-section. (c) B-B' cross-section. This structure was used for theoretical calculation.

Fig. 2. Overview of fabricated device with one beam for one side (A1 device). (a) Top view of the device. Beams support the center pad on both sides. An optical absorber was mounted on the center pad. The absorber has gold wires covered by sputtered Si.

Fig. 3. Beam pattern variations of Device A and B. Beam patterns are clipped, which is defined by the size of through-hole. The narrow beam length is 180 μm at one side in Device A. The total length of each beam is 180 μm in Device B.

Fig. 4. SEM images of the fabricated devices of Device A and B. The scale bars indicate 200 μm.

Fig. 5. SEM image (a) and absorption spectrum in the near-infrared region (b) of the fabricated optical absorber of sputtered Si/Au nanowire/Au thin film/Si. The absorption spectrum was obtained from the reflection spectrum measured by microspectroscopy of nanowire area.

Fig. 6. Analytical data points of stress along the beam. The axial stress at the three points, left edge, center, and right edge of the beam, in the cross-sectional view, are used for thermal stress evaluation. All points are half the beam thickness. The average of these three stresses is defined as the thermal stress for each cross-section.

Fig. 7. Experimental and analytical results for Device A. (a) Resonance curves of the two-beams device (A2) irradiated with near-infrared laser. Laser intensity varied from 0.5 to 1 mW. (b) Measured resonant frequencies and (c) resonant frequency change rates as a function of laser intensity P and the number of beams (A1-A3). The dotted line indicates analytical results calculated by FEM simulation. (d) Experimental and analytical resonant frequency change rate, and analytical thermal stress as a function of the number of beams (A1-A3).

Fig. 8. Experimental and analytical results for Device B. (a) Measured resonant frequency change rates as a function of laser intensity *P* and the number of corners (B1-B9). (b) Experimental and analytical resonant frequency change rate, and analytical thermal stress as a function of the number of corners (B1-B9).

Fig. 9. Analytical results of thermal stress distribution depending on a distance from the start point in cases of (a) B1 and (b) A2. Thermal stress was calculated as 3-point average of the cross-section of the beam.

Fig. 10. Analytical results of 3-point average stress depending on a distance from the start point and the total average of stress in cases of (a) B1 and (b) A2.

Fig. 11. Deformation distributions calculated by FEM simulation in cases of (a) B2 and (b) A1.

Fig. 12. Analytical results of thermal stress distribution depending on a distance from the start point in cases of B1, B2, and B3. Thermal stress was calculated as 3-point average of the cross-section of the beam. (a) Full range, (b) restricted range.

Fig. 13. Analytical maximum temperature of beam as a function of the number of corners.

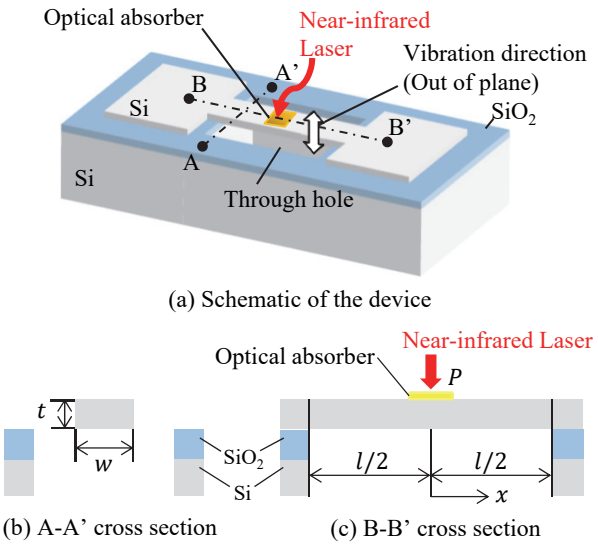

Fig. 1. (Color online)

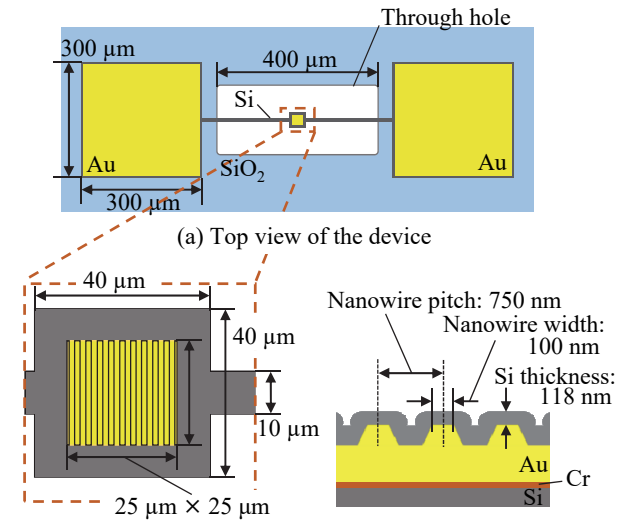

(a) Top view of the device

(b) Center pad (40 μm × 40 μm) and the optical absorber

(c) Cross section of the optical absorber

Fig. 2. (Color online)

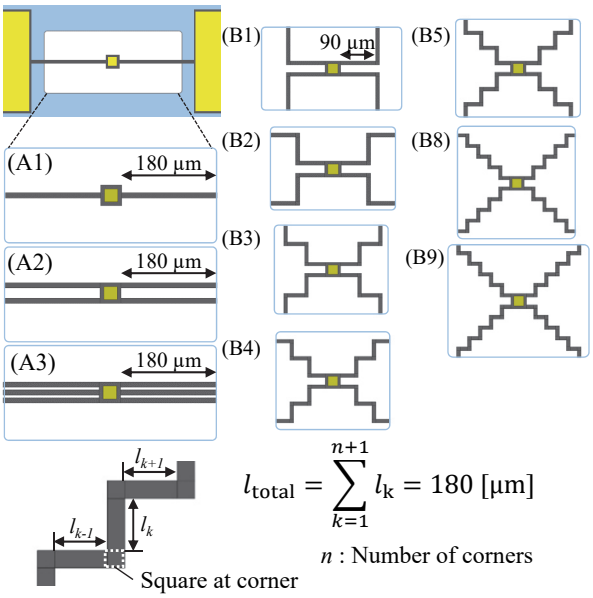

Fig. 3. (Color online)

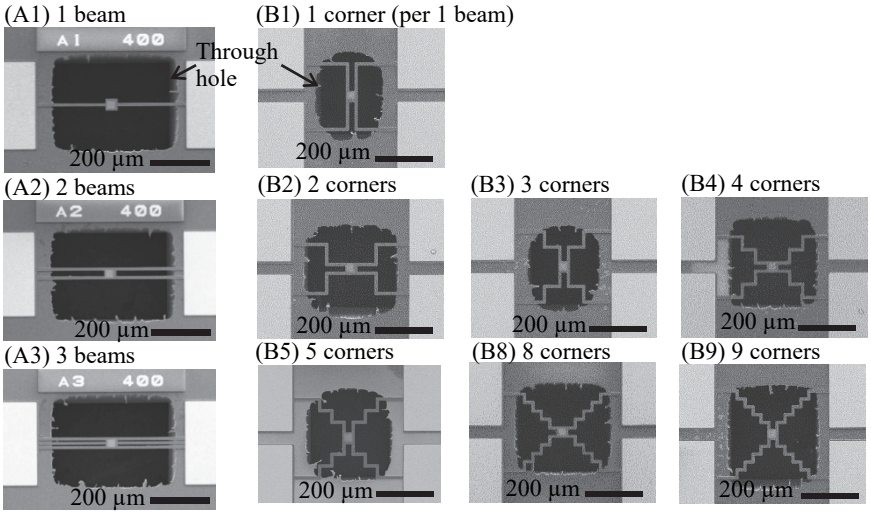
(A1) 1 beam
A1 400
Through hole
200 µm
(B1) 1 corner (per 1 beam)
200 µm
(A2) 2 beams
A2 400
200 µm
(B2) 2 corners
200 µm
(B3) 3 corners
200 µm
(B4) 4 corners
200 µm
(A3) 3 beams
A3 400
200 µm
(B5) 5 corners
200 µm
(B8) 8 corners
200 µm
(B9) 9 corners
200 µm

Fig. 4.

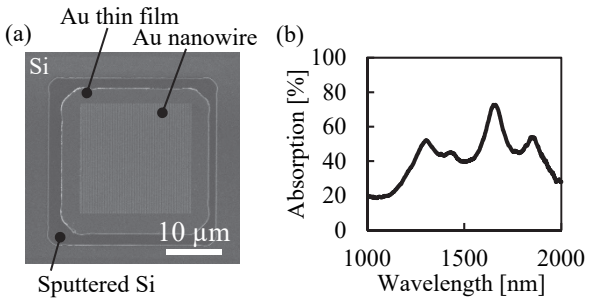
(a)
Au thin film
Au nanowire
Si
10 μm
Sputtered Si
(b)
Absorption [%]
100
80
60
40
20
0
1000
1500
2000
Wavelength [nm]

Fig. 5.

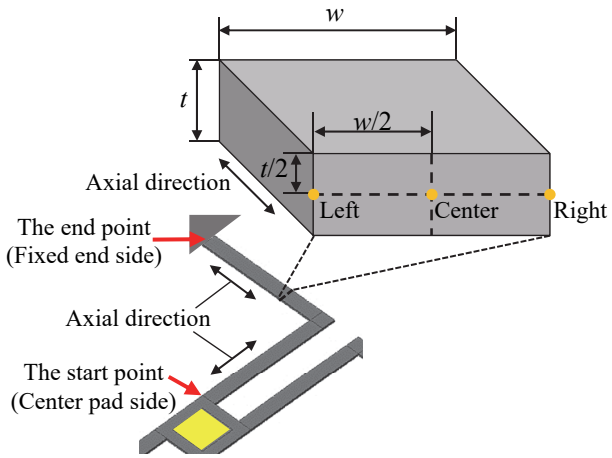

Fig. 6. (Color online)

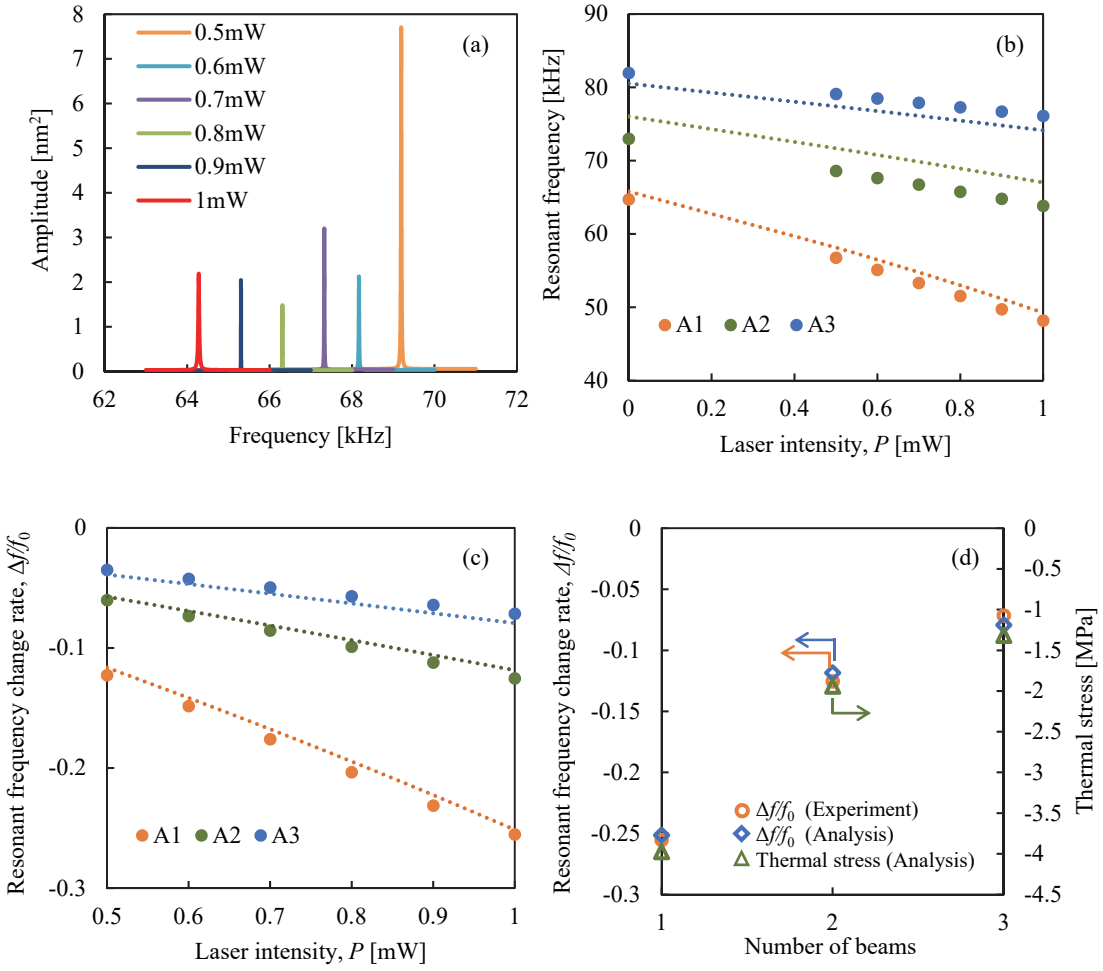

Fig. 7. (Color online)

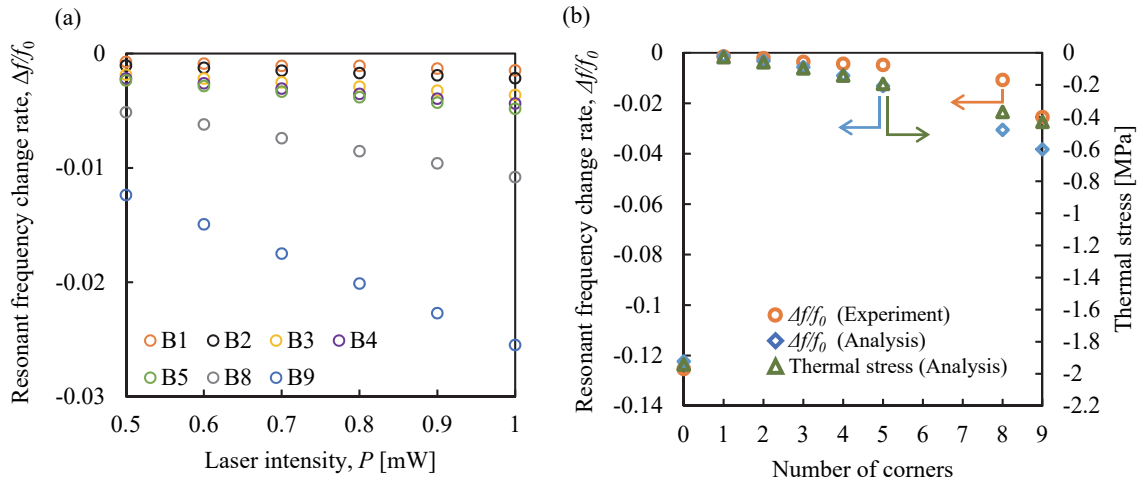

Fig. 8. (Color online)

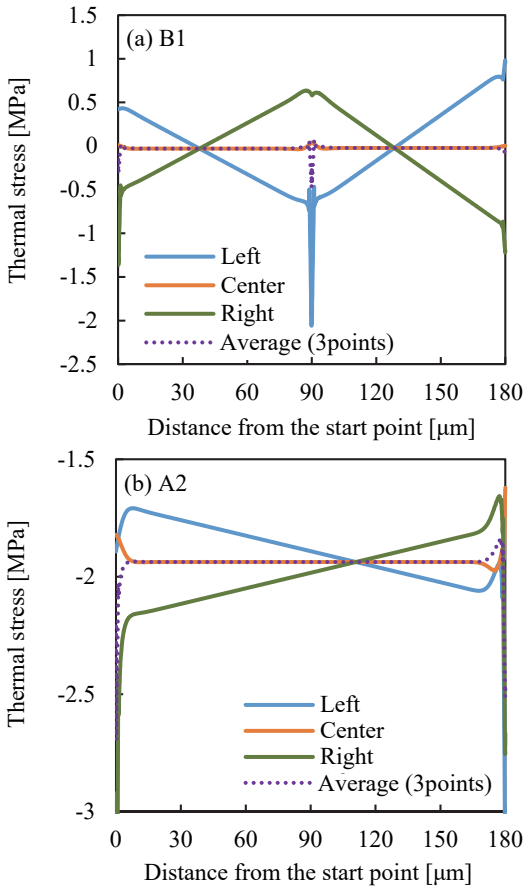

Fig. 9. (Color online)

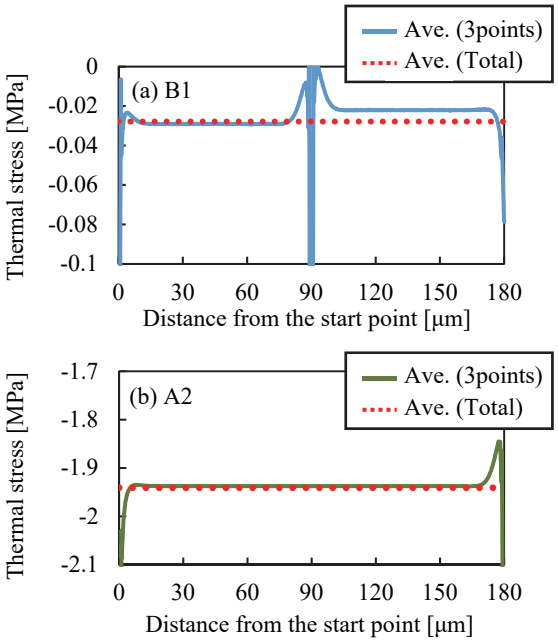

Fig. 10. (Color online)

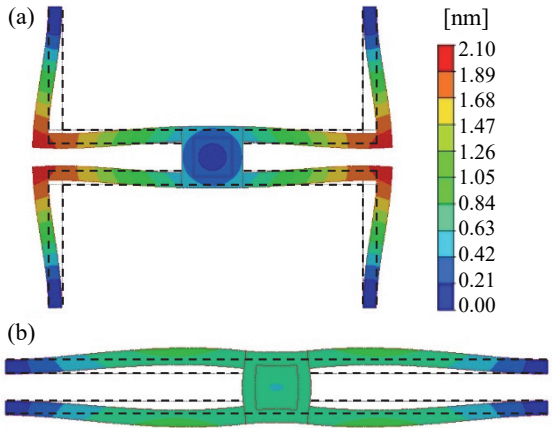

Fig. 11. (Color online)

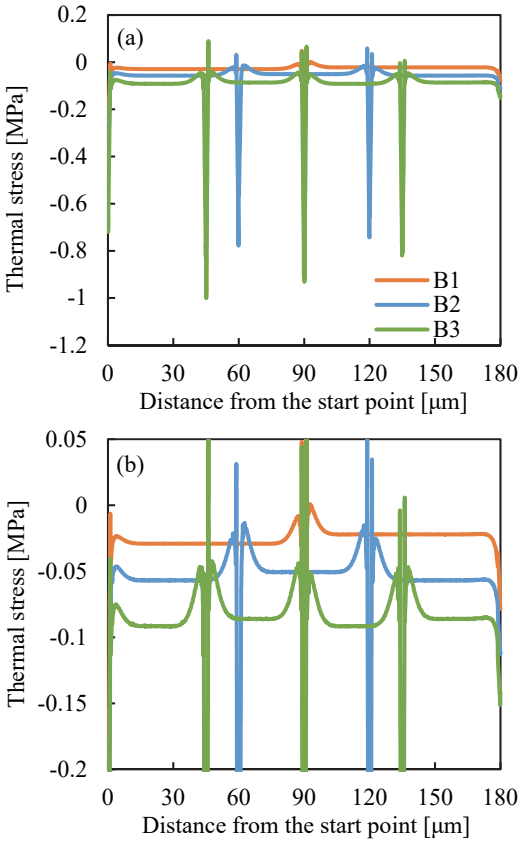

Fig. 12. (Color online)

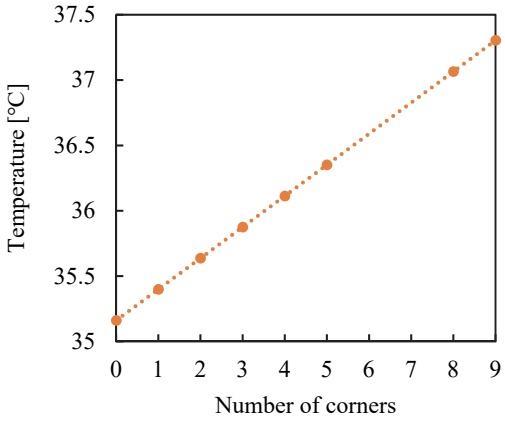
37.5
37
36.5
36
35.5
35
Temperature [°C]
0 1 2 3 4 5 6 7 8 9
Number of corners

Fig. 13.